Draft version January 6, 2018
Preprint typeset using LaTeX style AASTeX6 v. 1.0

NON-BLACKBODY DISKS CAN HELP EXPLAIN INFERRED AGN ACCRETION DISK SIZES

Patrick B. Hall, Ghassan T. Sarrouh
Department of Physics and Astronomy, York University, Toronto, ON M3J 1P3, Canada

Keith Horne
SUPA Physics and Astronomy, University of St. Andrews, North Haugh, St. Andrews KY16 9SS, Scotland, UK

ABSTRACT

If the atmospheric density $\rho_{\rm atm}$ in the accretion disk of an active galactic nucleus (AGN) is sufficiently low, scattering in the atmosphere can produce a non-blackbody emergent spectrum. For the same bolometric luminosity, at ultraviolet and optical wavelengths such disks have lower fluxes and apparently larger sizes as compared to disks that emit as blackbodies. We show that models with $\rho_{\rm atm}$ a sufficiently low fixed fraction of **the interior density** ρ can match the AGN STORM observations of NGC 5548, but produce disk spectral energy distributions (SEDs) that peak at shorter wavelengths than observed **in luminous AGN in general.** Thus, scattering atmospheres can contribute to the explanation for large inferred AGN accretion disk sizes, but are unlikely to be the only contributor. **In an appendix we present unified equations for the interior ρ and T in gas pressure dominated regions of a thin accretion disk.**

Keywords: accretion, accretion disks — galaxies: active — galaxies: individual (NGC 5548) — quasars: general

1. INTRODUCTION

The AGN STORM project has measured the wavelength-dependent time delays with which the accretion disk of NGC 5548 reverberates in response to emission from very close to the black hole (Edelson et al. 2015). The delays scale approximately as $t_{\rm delay}(\lambda) \propto \lambda$ (Fausnaugh et al. 2016, hereafter F16). This result has been interpreted as evidence for a disk that emits as a blackbody with a surface temperature profile $T_S(r) \propto r^{-1}$ (Starkey et al. 2017), since $t_{\rm delay} \propto r/c$ and **the peak wavelength of a blackbody spectrum follows** $\lambda \propto T^{-1}$**.** In contrast, a blackbody disk that releases locally the energy generated by viscous dissipation has a slower decrease of T_S toward larger radii, $T_S(r) \propto r^{-3/4}$ (Shakura & Sunyaev 1973, SS73; Novikov & Thorne 1973, NT73). A blackbody disk thus has $t_{\rm delay}(\lambda) \propto \lambda^{4/3}$; compared to NGC 5548, its time delays would drop more quickly toward shorter wavelengths.

Furthermore, the lags in NGC 5548 imply a disk $\simeq$3 times larger than expected for a standard thin disk with $L/L_{\rm Edd} \sim 0.1$ (F16). AGN accretion disks with radii 2× or more larger than expected **were first** inferred from microlensing observations of quasars (e.g., Eigenbrod et al. 2008; Morgan et al. 2010; Blackburne et al. 2011, 2015). **Larger than expected sizes have also been deduced** from photometric variability of quasars in Pan-STARRS (Jiang et al. 2016b) **and DES (Mudd et al. 2017). Proposed explanations for this discrepancy (see §4 of Hall et al. 2014) include an inhomogeneous disk with a range of temperatures at each radius (Dexter & Agol 2011; see also Cai et al. 2017), a long timescale for the disk to respond to changing illumination (Gardner & Done 2017), and an increase in the mean measured lag due to reverberation from diffuse gas at large scales (Cackett et al. 2017).**

Here we explore another mechanism that can help explain the above observations: a disk that deviates from a blackbody such that as the radius decreases $\lambda_{\rm peak}$ shifts to an increasingly shorter wavelength than for a blackbody of the same total flux. Electron scattering in the disk atmosphere of photons generated by free-free emission within the disk can produce an emergent spectrum with just such a shift (§2). As originally discussed in NT73 §5.10 and SS73 §3a, free-free emission produces shorter-wavelength photons deeper in the disk. If scattering is non-negligible in the disk atmosphere, such photons are less likely to escape; the emergent spectrum becomes non-blackbody **(e.g., Czerny & Elvis 1987).** To locally radiate all energy generated by viscous dissipation, the disk must heat up: as

scattering becomes sufficiently dominant (e.g., at low atmospheric densities), the peak of the spectrum shifts to shorter wavelengths and disks appear larger at a given wavelength than in the blackbody case **(e.g., Rauch & Blandford 1991). A small spectral shift in this direction (of insufficient magnitude to match observations) can occur in the emission from disk regions where electron scattering dominates (§5.10 of NT73 and §3a of SS73). A further shift in this direction (still of insufficient magnitude to match observations)** has been seen in previous work on disks with significant magnetic pressure support and thus low-density atmospheres (e.g., Blaes et al. 2006). This proposed explanation for large inferred accretion disk sizes is related to that of Abolmasov (2017), but distinct in that the electron scattering occurs in an accreting inflow in that work and in the disk atmosphere in this model. We explore in §3 what model parameters can produce a shift of the magnitude required to match the observations of NGC 5548 and discuss our results in §4.

2. TWO NON-BLACKBODY SPECTRAL MODELS

To examine how the spectrum from a disk with a scattering atmosphere varies with radius when gas pressure dominates, we consider two atmospheric density distributions: constant and exponential. In both cases we assume the atmospheres to be isothermal with height.

2.1. *Constant-density Atmosphere*

For the form of the emergent specific flux $F_\nu(r)$, we adopt the modified blackbody spectrum appropriate for isotropic scattering in a homogeneous medium (Rybicki & Lightman 1986; Equation 7 of Kawaguchi et al. 2004):

$$F_\nu(r) = \frac{2\pi B_\nu(T_S(r))}{1+\sqrt{1+\kappa_{es}/\kappa_{\nu,abs}(r)}} \tag{1}$$

where we use T_S to denote a characteristic disk surface temperature and where κ_{es} and $\kappa_{\nu,abs}$ are the electron-scattering opacity and the frequency-dependent absorption opacity, respectively. The factor of π comes from integrating the (assumed isotropic) emergent specific intensity over all solid angles.

The value of $T_S(r)$ is found by requiring local energy release. At each radius, the flux emitted over all wavelengths must equal the rate at which energy is generated per unit surface area: $\int F_\nu(r)\, d\nu = D(r)$ where $D(r)$ is given by Eq. A1. For $\kappa_{\nu,abs} \gg \kappa_{es}$, which occurs at sufficiently high densities or sufficiently low temperatures, $F_\nu = \pi B_\nu(T_S)$ and $T_S(r) = (D(r)/\sigma_{\rm sb})^{1/4}$. For $\kappa_{\nu,abs} \to 0$, which occurs at sufficiently low densities or sufficiently high temperatures, $F_\nu \to 2\pi B_\nu(T_S)\sqrt{\kappa_{\nu,abs}/\kappa_{es}}$, which can deviate strongly from a blackbody spectrum.

2.2. *Exponential Atmosphere*

Zel'dovich & Shakura (1969, ZS69) derive the expression for the specific flux emerging from a semi-infinite isothermal scattering atmosphere with an exponential density distribution $\rho(z) = \rho_1 e^{-(z-z_1)/h_1}$ where h_1 is the atmospheric scale height and z_1 is the height, above the disk plane, of the *edge* of the atmosphere. We take $h_1 = r^3 k_B T_S/GM\mu_p h$ where $h = (k_B T r^3/GM\mu_p)^{1/2}$ is the disk scale height (see the text following Eq. 2.28 in SS73). Thus, we have

$$h_1 = \left(\frac{k_B T_S^2 r^3}{GM\mu_p T}\right)^{1/2} = h\frac{T_S}{T}. \tag{2}$$

We define

$$k_{\nu,1} \equiv 3\kappa_{\rm es}\kappa_{\nu,abs1}h_1^2/\rho_1 \tag{3}$$

which is independent of density because $\kappa_{\nu,abs1}$, the absorption opacity at the edge of the atmosphere, is proportional to the local density ρ_1 (see §2.3). We can then write the emergent specific flux from this exponential atmosphere as

$$E_\nu(r) = \frac{\pi B_\nu(T_S(r))}{1+3\kappa_{\rm es}h_1\aleph_1/2k_{\nu,1}^{1/3}} \tag{4}$$

(Eq. A1.9 of ZS69, divided by 2 so that $E_\nu \to \pi B_\nu$ when electron scattering is unimportant; see Rybicki & Lightman 1986). In that equation, we define

$$\aleph_1 \equiv \frac{K_{1/3}(\frac{2}{3}k_{\nu,1}^{1/2}\rho_1^{3/2})}{k_{\nu,1}^{1/6}\rho_1^{1/2}K_{2/3}(\frac{2}{3}k_{\nu,1}^{1/2}\rho_1^{3/2})} > 0 \tag{5}$$

where the $K_a()$ are modified Bessel functions of the second kind. When ρ_1 is small the $\aleph_1$ term can dominate the denominator of E_ν and yield a spectrum differing greatly from a blackbody spectrum.

In the limit $k_{\nu,1}^{1/2}\rho_1^{3/2} \to \infty$, $\aleph_1 \to 0$ and $E_\nu \to \pi B_\nu$. In the limit $\rho_1 = 0$, $\aleph_1 \simeq 70/51$ to <1% accuracy and we can use the definition of $k_{\nu,1}$ to write the limiting form of E_ν as

$$E_\nu \simeq \pi B_\nu \frac{102 k_{\nu,1}^{1/3}}{210\kappa_{\rm es}h_1} \simeq \pi B_\nu \frac{17 k_{\nu,1}^{1/3}}{35\kappa_{\rm es}h_1} \simeq \left(\frac{512\kappa_{\rm es}\kappa_{\nu,abs1}h_1^2}{35\rho_1\kappa_{\rm es}^3 h_1^3}\right)^{1/3}\pi B_\nu \simeq \left(\frac{51\kappa_{\nu,abs1}}{35\rho_1\kappa_{\rm es}^2 h_1}\right)^{1/3}\pi B_\nu(T_S(r)) \tag{6}$$

which as expected is a factor of $\simeq 2^{1/3}$ lower than given at the end of Appendix 1 of ZS69.

2.3. *Parameter Dependences*

The non-blackbody frequency dependence of the spectrum emerging from the above atmospheres arises from the frequency dependence of the absorption opacity. We assume $\kappa_{\nu,abs}$ is given by the sum of free-free and bound-free absorption opacities and we approximate them as having the same frequency dependence (Meier 2012, §9.3.6.2). Defining $x \equiv h\nu/kT_S$, the specific absorption opacity can then be written

$$\kappa_{\nu,abs} = \kappa_{\rm bf+ff} = \kappa'_{*\rm f}\rho T_S^{-7/2}x^{-3}(1-e^{-x}) \tag{7}$$

with

$$\kappa'_{*\rm f} = (3.68\times10^{22}\ {\rm cm^2\ g^{-1}\ (g\ cm^{-3})^{-1}\ K^{7/2}})[X+Y+1180Zf(T)](1+X) \tag{8}$$

where the H, He, and metal mass fractions are $X = 0.71$, $Y = 0.27$, and $Z = 0.02$ for solar metallicity (Meier 2012, §9.3), and $f(T)$ is the fraction of metals that are not ionized (1 for neutral gas and 0 for fully ionized gas). The free-free opacity is dominated by electrons from H and He, while the bound-free opacity is dominated by electrons bound to metals. We take $f(T) = 0.5$, which yields $\kappa'_{*\rm f} = 8.04\times10^{23}$ cm^2 g^{-1} with the above mass fractions.

We also adopt $\kappa_{\rm es} = 0.2(1+X)$ cm^2 g^{-1} (Meier 2012, §9.3.6.1); more metal-rich gas with a lower X has fewer electrons per gram and therefore a lower electron scattering opacity.

We can now write out the full parameter dependencies of the specific flux $F_\nu(r)$ emergent from a constant-density atmosphere, again using $x \equiv h\nu/kT_S$ for convenience:

$$F_\nu(r) = \frac{(4k_B^3/c^2h^2)[x^3/(e^x-1)]T_S^3}{1+\sqrt{1+0.2x^3T_S^{7/2}/\kappa'_{*\rm f}\rho(1-e^{-x})[X+Y+1180Zf(T)]}} \tag{9}$$

where the $(1+X)$ dependencies in $\kappa_{\rm es}$ and $\kappa'_{*\rm f}$ have canceled out in the denominator.

The parameter dependencies of the specific flux $E_\nu(r)$ emergent from an exponential atmosphere can be written explicitly only in the low-density limit. That limit may not always apply, so we do not give the explicit form here.

In calculating ρ and T as part of determining $E_\nu(r)$ or $F_\nu(r)$, we adopt a mean mass per particle of

$$\mu_p = \frac{m_p}{2X+0.75Y+Z[0.56-0.5f(T)]} \tag{10}$$

(Meier 2012, §9.3.1.1) where m_p is the proton mass. That expression is appropriate for gas which is completely ionized in H and He but in which metals range from neutral to fully ionized. For **the parameters given above**, $\mu_p = 0.614m_p$.

2.4. *Calculating T_S, the emergent spectrum,* **and mean measured radii**

The emergent F_ν from a disk atmosphere depends on the opacity and thus the density *in the atmosphere*, which will be lower than the average interior density. We adopt an atmospheric density $\rho_{\rm atm}(r)$ which is a constant fraction of the interior density $\rho(r)$. To find $F_\nu(r)$ or $E_\nu(r)$ thus requires knowing the gas density $\rho(r)$, **which for gas pressure dominated regions of an AGN accretion disk requires knowing the disk interior temperature $T(r)$. In such regions we use the analytic expressions for $T(r)$ and $\rho(r)$ derived in the Appendix. For radiation pressure dominated disk regions, we calculate $\rho(r)$ and $T(r)$ using Eq. 2.11 and 2.12 of SS73, respectively.**[1] **The transition between these two regions is the radius at which they yield equal values of $\rho(r)$. We adopt radiation-pressure dominated values of $\rho(r)$ and $T(r)$ interior to that radius, and gas-pressure dominated values exterior to that radius.**

Once a value for the atmospheric density $\rho_{\rm atm}(r)$ as a fraction of $\rho(r)$ is adopted, the characteristic disk surface temperature $T_S(r)$ is determined iteratively by requiring $\int F_\nu(\rho_{\rm atm}(r), T_S(r))d\nu = D(r)$ for a constant-density

[1] **There is a typo in Eq. 2.12 of SS73, which reads $r^{-3/4}$ instead of the correct value of $r^{-3/8}$; see Eq. 5.9.10 of NT73.**

atmosphere, or $\int E_\nu(\rho_{\rm atm}(r), T_S(r))d\nu = D(r)$ for an exponential-density atmosphere. **Once $T_S(r)$ is known, the emergent spectrum as a function of ν is calculated as the area-weighted integral of F_ν or E_ν over the disk.** We present results for a range of atmospheric densities for both non-blackbody spectral models considered.

For comparison with microlensing and reverberation mapping observations, we assume a face-on disk and calculate the flux-weighted and response-function-weighted (Cackett et al. 2007) mean radii, respectively:

$$r_f(\lambda) = \frac{\int_{r=r_{\rm in}}^{r=\infty} r\ X_\lambda(r)\ r\ dr}{\int_{r=r_{\rm in}}^{r=\infty} X_\lambda(r)\ r\ dr} \quad \text{and} \quad r_r(\lambda) = \frac{\int_{r=r_{\rm in}}^{r=\infty} r\ \psi_\lambda(r)\ r\ dr}{\int_{r=r_{\rm in}}^{r=\infty} \psi_\lambda(r)\ r\ dr} \tag{11}$$

where $X_\lambda(r) = B_\lambda(r)$ for a standard disk, $F_\lambda(r)$ for a constant-density scattering atmosphere (§2.1), and $E_\lambda(r)$ for an exponential scattering atmosphere (§2.2), and $\psi_\lambda(r)$ is the response function (for a derivation, see Horne et al. in preparation). We assume instantaneous thermalization and re-emission of incident illumination. We refer to these wavelength-dependent radii collectively as $r(\lambda)$ and express them in light-days for comparison with time lag observations; the mean time lag is insensitive to disk inclination (Fig. 1 of Starkey et al. 2017).

3. COMPARISON TO NGC 5548 OBSERVATIONS

To compare with the observations of NGC 5548, we adopt a cosmology with $\Omega_M = 0.28$, $\Omega_\Lambda = 0.72$, and $H_0 = 70$ km s^{-1} Mpc^{-1} (Komatsu et al. 2011), which yields a luminosity distance of 74.5 Mpc at its redshift of $z = 0.017175$ (De Rosa et al. 2015). We model a disk with viscosity parameter $\alpha = 0.1$ around a non-rotating black hole of mass $M = (6.66 \pm 2.17) \times 10^7\ M_\odot$ (Pei et al. 2017). The Schwarzschild radius is $R_{\rm Sch} = 1.97 \times 10^{13}$ cm = 657 light-seconds and the Eddington limit is $L_{\rm Edd} = 4\pi GM\mu_e c/\sigma_T = 9.79 \times 10^{45}$ erg s^{-1}, where $\mu_e = 2m_p/(1+X)$ is the mean mass per electron. The corresponding Eddington mass accretion limit is $\dot{M}_{\rm Edd} = L_{\rm Edd}/(0.1\eta_{0.1}c^2) = 9.39\eta_{0.1}^{-1} \times 10^{25}$ g s^{-1}; for our non-rotating black hole with $r_{in} = 3R_{\rm Sch}$, we adopt the appropriate nonrelativistic value of $\eta_{0.1} = 5/6$ (Frank et al. 2002). NGC 5548 has bolometric luminosity $\simeq 10^{44.83}$ erg s^{-1} (Woo & Urry 2002) and so we adopt $L/L_{\rm Edd} = 0.069$.

We calculate $X_\lambda(r)$ for $3 < r/R_{\rm Sch} < 4000$ for a range of atmospheric densities from $\log(\rho_{\rm atm}/\rho) = 0$ to -5 for both scattering atmosphere models, and then calculate $r(\lambda)$ for each. **The transition between radiation- and gas-pressure dominated regions occurs at $r \simeq 223R_{\rm Sch}$, as compared to $r \simeq 237R_{\rm Sch}$ predicted by SS73 Eq. 2.17 or NT73 Eq. 5.9.9 for the NGC 5548 parameters adopted in this section. The difference arises because the values of $T(r)$ and $\rho(r)$ in gas-pressure dominated regions differ slightly from what is assumed in the approximations used in deriving those equations (see the end of the Appendix).**

In Figure 1, for comparison with Figure 5 of F16, we plot the wavelength-dependent relative disk reverberation time lag, estimated from the response-function-weighted mean radii $r(\lambda) - r(1367\ \text{Å})$ (solid lines) for blackbody disks (black) and scattering-atmosphere disks with constant density (red) and exponential density (cyan), all with $L = 0.069L_{\rm Edd}$. **At $\rho_{atm}/\rho = 0$, the relative time lags lie above the blackbody disk value at 1000 Å $\lesssim \lambda \lesssim$ 6000 Å, and below it at other wavelengths. As ρ_{atm}/ρ decreases, the relative time lags decrease further at $\lambda \lesssim$ 1000 Å and increase at longer wavelengths until they are above the blackbody disk values at all wavelengths plotted (last three panels).** As expected from §2, at sufficiently low $\rho_{\rm atm}$ the time lags at each radius approach limiting values for an exponential-density atmosphere and continue to increase for a constant-density atmosphere.

The dotted lines in Figure 1 show results for flux-weighted mean radii, to illustrate the relative disk sizes expected in microlensing observations. Such radii are smaller than response-function-weighted radii because the latter give high weight to radii which have not reached the Rayleigh-Jeans limit at a given λ.

Scattering atmospheres with sufficiently low relative densities can explain the observed wavelength-dependent reverberation signal in NGC 5548. **For response-function-weighted radii with $\log(\rho_{\rm atm}/\rho)$=−4, for an exponential-density atmosphere we find $r_r(\lambda) \propto \lambda^{1.14\pm0.02}$, and for a constant-density atmosphere we find $r_r(\lambda) \propto \lambda^{1.00\pm0.02}$ at $1000 < \lambda < 4000$ Å and $r_r(\lambda) \propto \lambda^{0.82\pm0.02}$ at $\lambda > 4000$ Å.**

In Figure 2, we plot the flux density f_ν vs. ν from an annulus at **60** $R_{\rm Sch}$, to illustrate how the emergent spectrum changes with $\rho_{\rm atm}/\rho$ for both scattering atmosphere models. The middle right panel includes color-corrected blackbody curves with peak wavelengths matching both models. Because both models have more flux at short and long wavelengths than the matching color-corrected blackbody curves, modeling disk emission with the latter (e.g., Davis et al. 2006; Done et al. 2012) will not fully reproduce emission from these scattering atmosphere models.

In the left panel of Figure 3, we plot f_ν for NGC 5548 vs. expectations for disks with $\rho_{\rm atm} = 10^{-4}\rho$. The constant-density model overpredicts f_ν by less than a factor of 3 at the wavelengths plotted. However, panel 5 of Figure 4 shows that the integrated λF_λ for such a disk peaks at much shorter wavelengths than for blackbody disks. **and is a poor match to the optical-UV-X-ray SED of NGC 5548 (Mehdipour et al. 2015). Note that panel 1 of Figure 4 shows the expected deviation of even a standard thin disk's SED**

from a sum of blackbodies, as seen in Figure 5.10.1 of NT73 and Figure 3 of SS73. However, this deviation is due almost entirely to emission from radii $r < 20R_{\rm Sch}$. The differences are small at larger radii; as an example, the SED from $r > 60R_{\rm Sch}$ is shown in panel 1.

For objects where such SEDs conflict with observations, winds from the disk may reduce $\dot{M}$ at small radii and thus the luminosity from the inner disk, preventing the SED from peaking at too short a wavelength (Slone & Netzer 2012; Laor & Davis 2014; see also Proga 2005). Alternatively, at small radii the disk may transition to a thick torus whose emission peaks in the far or extreme ultraviolet **(e.g., §2 of Gardner & Done 2017). As a purely illustrative limiting case of the above, in the right panel of Figure 3 and the lower left panel of Figure 4 we show SEDs for models with $\log(\rho_{\rm atm}/\rho) = -4$ but from disk radii $r > 60R_{\rm Sch}$ only ($r > 11$ light-hours). These SEDs show the relative fluxes of the inner and outer disks at those wavelengths. As shown in Figure 7 (left panel), our model's predicted mean relative disk reverberation time lags at $\lambda > 1367$ AA (solid lines) are not greatly changed if the emission from $r < 60R_{\rm Sch}$ is excluded (dashed lines). Absolute time lag predictions, in contrast, are strongly dependent on the UV emission properties of the inner disk. Figure 7 (right panel) shows that our model's predicted mean *absolute* disk reverberation time lags with emission from $r < 60R_{\rm Sch}$ excluded (dashed lines) are closer to the AGNSTORM observations of NGC 5548 than our model's predictions including the full disk (solid lines). Thus, models which suppress optical/UV emission disk from radii $r < 60R_{\rm Sch}$ to better fit the constraints of observed AGN SEDs may be able to simultaneously match inferred relative and absolute disk sizes.**

4. DISCUSSION

If the atmospheric density in an AGN accretion disk is sufficiently low, scattering in the atmosphere can produce a non-blackbody emergent spectrum. Disks with these scattering atmospheres have lower brightness temperatures and higher colour temperatures at ultraviolet and optical wavelengths than the blackbody temperature of a disk of the same bolometric luminosity; thus, they can in principle reconcile disk theory sizes and flux sizes with microlensing sizes (see, e.g., §1 of Hall et al. 2014).

The AGN STORM observations of NGC 5548 are **in many — but not all — aspects consistent with a disk with a constant-density scattering atmosphere with density $\rho_{\rm atm} = 10^{-4}\rho$. In particular, although the observed optical-UV-X-ray SED of NGC 5548 is not well matched by that model (Figure 4), the observed optical-UV flux from NGC 5548 is lower than in all models at our adopted Eddington ratio of $L = 0.069L_{\rm Edd}$ (Figure 3). That Eddington ratio is based on the bolometric luminosity from Woo & Urry (2002), which was found by summing multiwavelength flux values for NGC 5548 from the literature. Contamination of flux measurements by the host galaxy, particularly at infrared wavelengths, could mean that the true Eddington ratio is lower than we have assumed, which would help explain the lower optical-UV flux level (e.g., Gardner & Done (2017) adopt $L = 0.040L_{\rm Edd}$).**

As a consistency check, we note that the physical density corresponding to $\rho_{\rm atm} = 10^{-4}\rho$ in our NGC 5548 disk models is 10^{-10}-10^{-14} g cm^{-3} at 4-4000 $R_{\rm Sch}$ from the black hole, with a minimum at 8.5 $R_{\rm Sch}$. The vertical length scale corresponding to $\tau_{es} = 1$ at such densities is h_{es}=10^{10}-10^{14} cm. The atmospheric scale height/radius ratio h_{es}/r peaks at 0.18 at 8.5 $R_{\rm Sch}$ and has a value $h_{es}/r < 10^{-2}$ at $40 < r/R_{\rm Sch} < 4000$. A self-consistent atmosphere model must have $h_{es}/r \ll 1$, so our constant-density model results at $r < 40R_{\rm Sch}$ should be treated with caution. For an exponential atmosphere with $\rho_{\rm atm} = 10^{-4}\rho$ and scale height h_1 (Eq. 2), we find at all radii that $h_1/r \lesssim 6 \times 10^{-5}$, so $h_1 < h_{es}$. Thus, the semi-infinite exponential atmosphere model we use (§2.2) is a reasonable approximation. Compared to an infinite exponential atmosphere, it neglects a region of optical depth only $\tau = \kappa_{\rm es}\rho_{\rm atm}h_1 < 1$.

We can compare our $\log(\rho_{\rm atm}/\rho)$=−4 model predictions to the results of microlensing observations. For flux-weighted radii with $\log(\rho_{\rm atm}/\rho)$=−4, for an exponential-density atmosphere we find $r_f(\lambda) \propto \lambda^{1.09\pm0.02}$, and for a constant-density atmosphere we find $r_r(\lambda) \propto \lambda^{0.84\pm0.02}$. In the Einstein Cross Eigenbrod et al. (2008) found flux-weighted radii $r_f \propto \lambda^{1.2\pm0.3}$. In the quasar HE 1104−1805 Blackburne et al. (2015) found $r_f \propto \lambda^{1.0(+0.3,-0.56)}$ and a size larger than expected by a factor of 4 at 1900 Å, as compared to our prediction of a factor ~ 3 (Figure 5). In a sample of 11 quasars, Blackburne et al. (2011) found $r_f \propto \lambda^{0.17\pm0.15}$ and a size larger than expected by a factor of 10^{+7}_{-5} at 1736 Å, as compared to our prediction of a factor ~ 3. The results from first two studies above are reasonably consistent with both the theoretical prediction of $r_f \propto \lambda^{4/3}$ and with our model results; see Hall et al. (2014) for further discussion of the Blackburne et al. (2015) results.

For $\rho_{\rm atm}$ values low enough for scattering to help explain the inferred large sizes of AGN accretion disks, some

mechanism must support the low-density atmosphere above the disk; magnetic pressure support is an obvious possibility. Blaes et al. (2006) have shown that accounting for magnetic pressure yields a more extended accretion disk atmosphere which shifts the emergent SED in a similar manner to our Figure 4; see also Begelman & Pringle (2007), Davis et al. (2009), and Tao & Blaes (2013). Such studies found photospheric densities of $\rho_{\rm atm} \simeq 10^{-3}\rho$ (Figure 6 of Blaes et al. 2006) and $\rho_{\rm atm} \simeq 2 \times 10^{-3}\rho$ (Figure 3 of Davis et al. 2009) in disks around stellar-mass black holes. It remains to be seen if disks around supermassive black holes can reach the lower atmospheric densities required for scattering atmospheres to explain large apparent AGN disk sizes.

The models discussed here predict that scattering atmospheres of different densities will yield different apparent disk sizes and $t_{\rm delay}(\lambda) \propto \lambda^x$ slopes x. **In addition, at low atmospheric densities these models predict sizes relative to blackbody disks which have maxima at $\lambda \lesssim 1000$ Å and decrease towards approximately unity at longer wavelengths (Figure 5).** Overall, disk sizes are predicted to be more anomalous in the ultraviolet than in the optical, and response-function-weighted radii to be more discrepant from their corresponding blackbody values than flux-weighted radii. However, we have not accounted for specific features in the bound-free opacity such as the temperature-dependent iron opacity bump (see Jiang et al. 2016a and references therein) or the Balmer and Paschen edges. In particular, if the disk atmospheres contain sufficient H I, disk sizes and time lags at the wavelengths of H I edges may differ noticeably from our predictions. It remains to be seen whether or not such an effect can explain the discrepant U-band lags noted in F16.

If scattering atmospheres are important in AGN disks, dependences of the scattering atmosphere properties on AGN parameters such as M and $\dot{M}$ may help explain why SDSS quasars do not show the expected trends of continuum color or emission line properties with such parameters (Bonning et al. 2007, 2013).

The models discussed here do not by themselves match all AGN observations. They produce SEDs that peak at shorter wavelengths than observed in many AGN. **While the models can show a non-zero lag between X-ray and ultraviolet emission (e.g., Figure 1 for $\log(\rho_{atm}/\rho) = -4$), as seen in NGC 2617 (Shappee et al. 2014) and NGC 4151 (Edelson et al. 2017), the slow increase in the lag from ultraviolet to optical wavelengths in those objects is not reproduced. A disk that transitions at small radii to a torus emitting at extreme ultraviolet wavelengths (e.g., Gardner & Done 2017; Edelson et al. 2017) may alleviate these problems.**

We thank the referee and B. Czerny, C. Done, C. Knigge, J. Matthews, H. Netzer, and D. Starkey for discussions. PH and GS acknowledge the support of the Natural Sciences and Engineering Research Council of Canada (NSERC), funding reference number 2017-05983. KH acknowledges support from STFC grant ST/M001296/1.

Software: MATLAB

APPENDIX

A. DENSITY AND TEMPERATURE IN GAS PRESSURE DOMINATED REGIONS OF AN ACCRETION DISK

We desire equations for ρ and T in regions of an accretion disk where $P = P_{gas}$ and $\kappa = \kappa_{\rm es} + \kappa_{\rm bf+ff}$. For comparison with SS73, we use cgs units and neglect general relativistic corrections.

We will require $D(r)$, the rate at which mechanical energy is transformed into heat energy per unit surface area over both sides of the disk. Following Frank et al. (2002), we write

$$D(r) = \frac{3G\dot{M}M}{8\pi r^3}\left(1 - \sqrt{\frac{r_{in}}{r}}\right) = \frac{3G\dot{M}M}{8\pi r^3} f(r). \tag{A1}$$

where M is the black hole mass, $\dot{M}$ is the mass accretion rate, and $f(r)$ involves the innermost disk radius r_{in}.

To find ρ, we begin with the radiative energy transport equation $\sigma_{\rm sb}T^4 = \kappa\Sigma F$ (NT73 Eq. 5.8.1c) where T is the interior disk temperature, $\kappa = \kappa_{\rm es} + \kappa_{\rm bf+ff}$ is the opacity, Σ is the mass surface density, and $F(r)$ is the total surface flux emitted at r. We take $\kappa_{\rm bf+ff} = \kappa'_{*\rm f}\rho T^{-7/2}$ so that $\kappa'_{*\rm f}$ has units of cm^2 g^{-1} (g cm^{-3})$^{-1}$ K$^{7/2}$. We assume that energy released is radiated locally, so that $F(r) = D(r)$. Substituting in for κ, $\Sigma = 2\rho h$, and $F(r) = D(r)$,

$$\sigma_{\rm sb}T^4 = (\kappa_{\rm es} + \kappa'_{*\rm f}\rho T^{-7/2}) \times 2\rho h \times (3G\dot{M}Mf(r)/8\pi r^3). \tag{A2}$$

The above is a quadratic equation for ρ. We substitute for the disk half-thickness $h = (Pr^3/\rho GM)^{1/2}$ (NT73 Eq. 5.8.1a) rewritten using $P = \rho k_B T/\mu_p$ as $h = (k_B T r^3/GM\mu_p)^{1/2}$, where μ_p is the mean mass per particle in grams. The quadratic equation and its solution are:

$$a_q\rho^2 + b_q\rho + c_q = 0 \text{ with } a_q = \kappa'_{*\rm f}T^{-7/2}\ ;\ b_q = \kappa_{\rm es}\ ;\ c_q = -4\pi\sigma_{\rm sb}T^{7/2}\mu_p^{1/2}r^{3/2}/3(k_BGM)^{1/2}\dot{M}f(r) \tag{A3}$$

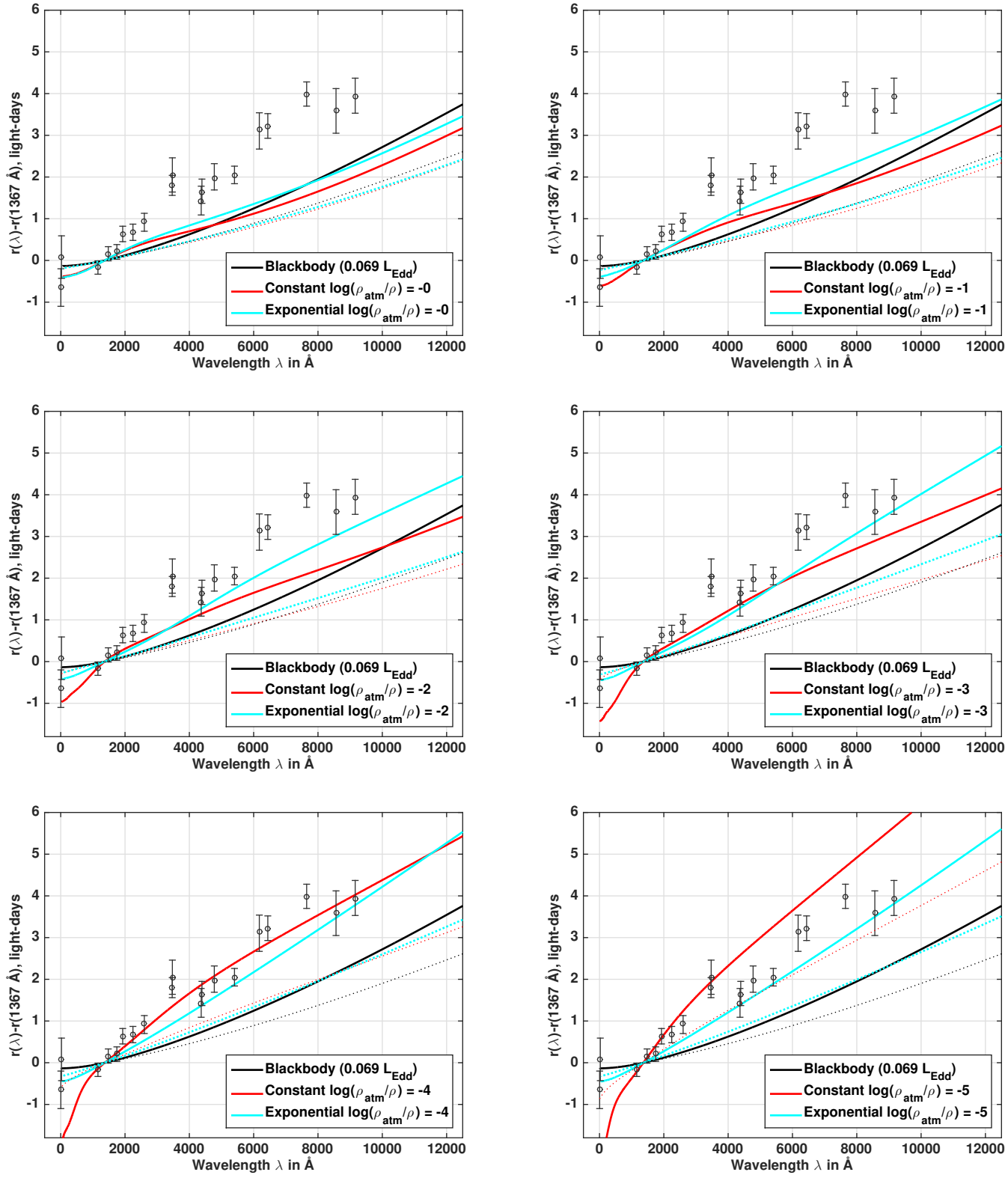

Figure 1. The wavelength-dependent relative disk reverberation time lag estimated from the response-function-weighted mean radius $r(\lambda) - r(1367\ \text{Å})$ (solid lines), overplotted on the wavelength-dependent time lag data for NGC 5548 (points and error bars, from F16; note that the U-band points just shortward of 4000 Å are known to be discrepant). Dotted lines show results for flux-weighted mean radii, to illustrate the relative disk sizes expected in microlensing observations. We plot curves for blackbody disks (black) and scattering-atmosphere disks with constant density (red) and exponential density (cyan), all with $L = 0.069 L_{\rm Edd}$. The density of the scattering atmosphere relative to the average interior density is $\log(\rho_{atm}/\rho) = 0$ and -1 (top), -2 and -3 (middle), and -4 and -5 (bottom). **At $\rho_{atm}/\rho = 0$, the relative time lags lie above the blackbody disk value at 1000 Å $\lesssim \lambda \lesssim$ 6000 Å, and below it at other wavelengths. As ρ_{atm}/ρ decreases, the relative time lags decrease further at $\lambda \lesssim$ 1000 Å and increase at longer wavelengths until they are above the blackbody disk values at all wavelengths plotted (last three panels).**

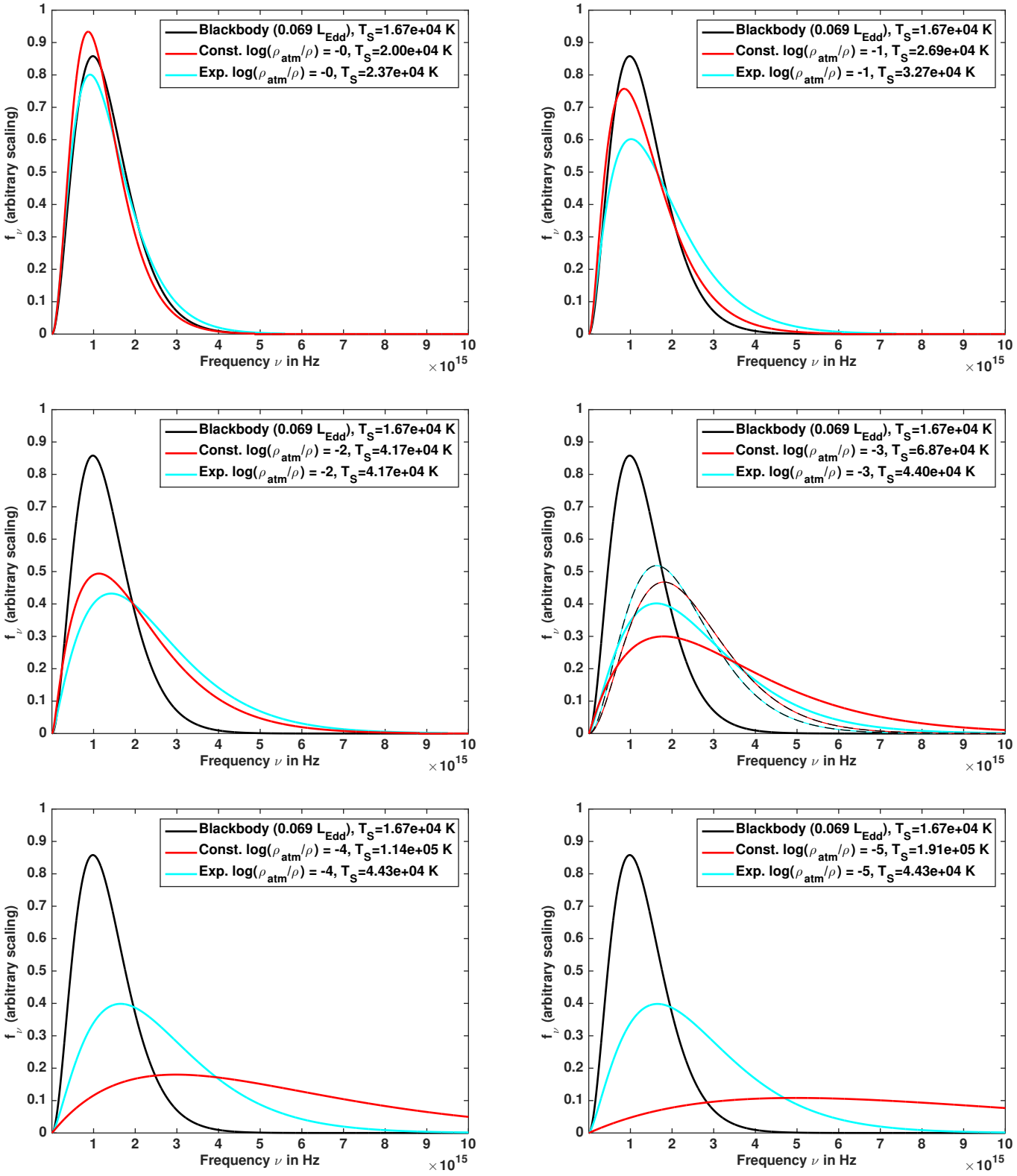

Figure 2. Flux density f_ν from an annulus at **60** $R_{\rm Sch}$ in a disk with $L = 0.069 L_{\rm Edd}$ around NGC 5548. Panel layout and color key are as in Figure 1. The middle right panel includes color-corrected blackbody curves with the same peak wavelengths as the constant-density and exponential models **(dashed red-black with** $T_S = 3.07$**e+04 K and dashed cyan-black with** $T_S = 2.77$**e+04 K, respectively).**

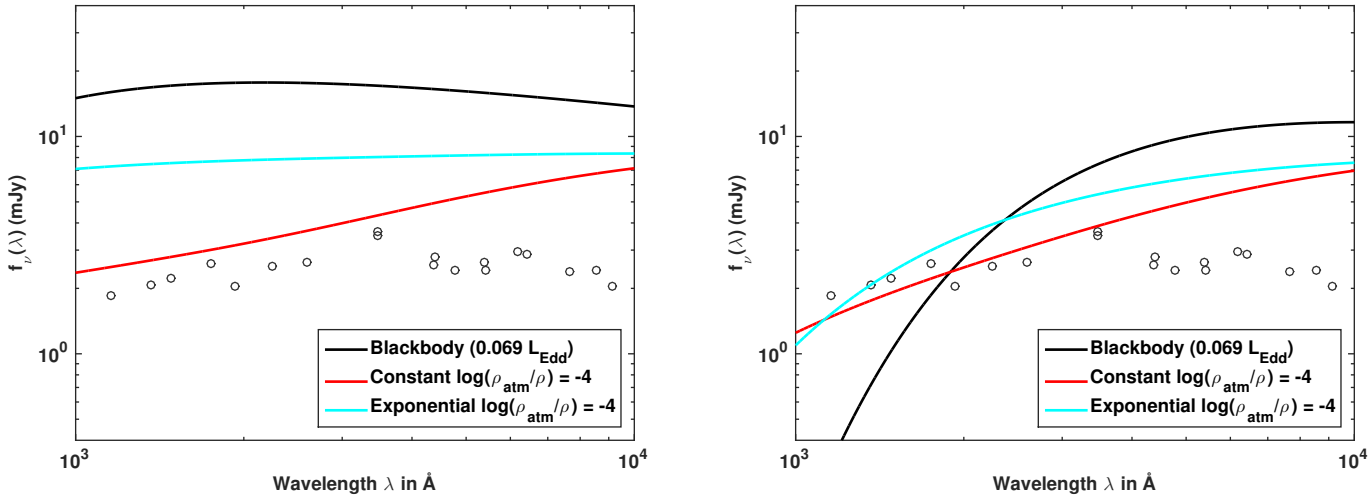

Figure 3. In comparison to the average observed f_ν values from Figure 11 of Starkey et al. (2017), we plot the predicted flux density from face-on accretion disks with $L = 0.069 L_{\rm Edd}$ and $\log(\rho_{\rm atm}/\rho) = -4$ in NGC 5548, with the same color key as Figure 1. The left panel shows f_ν from the entire disk; the right shows f_ν from $r > 60 R_{\rm Sch}$ ($r > 11$ light-hours) only.

$$\rho = \frac{\kappa_{\rm es} T^{7/2}}{2\kappa'_{*\rm f}} \left[-1 + \sqrt{1 + \frac{16\pi\kappa'_{*\rm f}\sigma_{\rm sb}(\mu_p/k_B)^{1/2}}{3\kappa_{\rm es}^2 (GM/r^3)^{1/2}\dot{M} f(r)}} \right] \tag{A4}$$

To find T, we use two expressions for the vertically integrated shear stress, $W = 2h\alpha P = 2h\alpha\rho k_B T/\mu_p$ (NT73 Eqs. 5.7.5d and 5.8.1b) and $W = [f(r)\dot{M}(GM/r^3)^{1/2}]/2\pi$ (NT73 Eq. 5.6.14a), to find a second equation relating ρ and T:

$$\rho = \frac{f(r)\dot{M}(GM/r^3)}{4\pi\alpha(k_B T/\mu_p)^{3/2}}. \tag{A5}$$

Equating Eqs. A4 and A5 and solving for T, we find:

$$T = \left[\frac{\kappa'_{*\rm f} f(r)\dot{M}(GM/r^3)}{2\pi\kappa_{\rm es}\alpha(k_B/\mu_p)^{3/2}} \left(-1 + \sqrt{1 + \frac{16\pi\kappa'_{*\rm f}\sigma_{\rm sb}(\mu_p/k_B)^{1/2}}{3\kappa_{\rm es}^2 (GM/r^3)^{1/2}\dot{M} f(r)}} \right)^{-1} \right]^{1/5} \tag{A6}$$

We have verified that these expressions have the correct numerical coefficients and dependencies on r, M, $\dot{M}$, and α in the limits $\kappa'_{*\rm f} \ll \kappa_{\rm es}$ and $\kappa'_{*\rm f} \gg \kappa_{\rm es}$. The limiting solutions are approached slowly; e.g., the disk T is higher at large radii (SS73 region c) than predicted by the limiting solution because T has a steeper radial dependence in region b than in region c, resulting in the limiting T in region c being approached from above.

In disk regions where $P = P_{rad} + P_{gas}$ and $\kappa = \kappa_{\rm es}$, we searched for analytic solutions for ρ and T but found only implicit equations.

REFERENCES

Abolmasov, P. 2017, A&A, 600, A79

Begelman, M. C., & Pringle, J. E. 2007, MNRAS, 375, 1070

Blackburne, J. A., Pooley, D., Rappaport, S. & Schechter, P. L. 2011, ApJ, 798, 95

Blackburne, J. A., Kochanek, C. S., Chen, B., Dai, X., & Chartas, G. 2015, ApJ, 798, 95

Blaes, O. M., Davis, S. W., Hirose, S., Krolik, J. H., & Stone, J. M. 2006, ApJ, 645, 1402

Bonning, E. W., Cheng, L., Shields, G. A., Salviander, S., & Gebhardt, K. 2007, ApJ, 659, 211

Bonning, E. W., Shields, G. A., Stevens, A. C., & Salviander, S. 2013, ApJ, 770, 30

Cackett, E. M., Horne, K., & Winkler, H. 2007, MNRAS, 380, 669

Cackett, E. M., Chiang, C.-Y., McHardy, I., et al. 2017, ArXiv e-prints, arXiv:1712.04025

Cai, Z. Y., Wang, J.-X., Zhu, F.-F., et al. 2017, ArXiv e-prints, arXiv:1711.06266

Czerny, B., & Elvis, J. E. 1987, ApJ, 321, 305

Davis, S. W., Blaes, O. M., Hirose, S., & Krolik, J. H. 2009, ApJ, 703, 569

Davis, S. W., Done, C., & Blaes, O. M. 2006, ApJ, 647, 525

De Rosa, G., Peterson, B. M., Ely, J., et al. 2015, ApJ, 806, 128

Dexter, J., & Agol, E. 2011, ApJL, 727, L24

Done, C., Davis, S. W., Jin, C., Blaes, O., & Ward, M. 2012, MNRAS, 420, 1848

Edelson, R., Gelbord, J. M., Horne, K., et al. 2015, ApJ, 806, 129

Edelson, R., Gelbord, J., Cackett, E., et al. 2017, ApJ, 840, 41

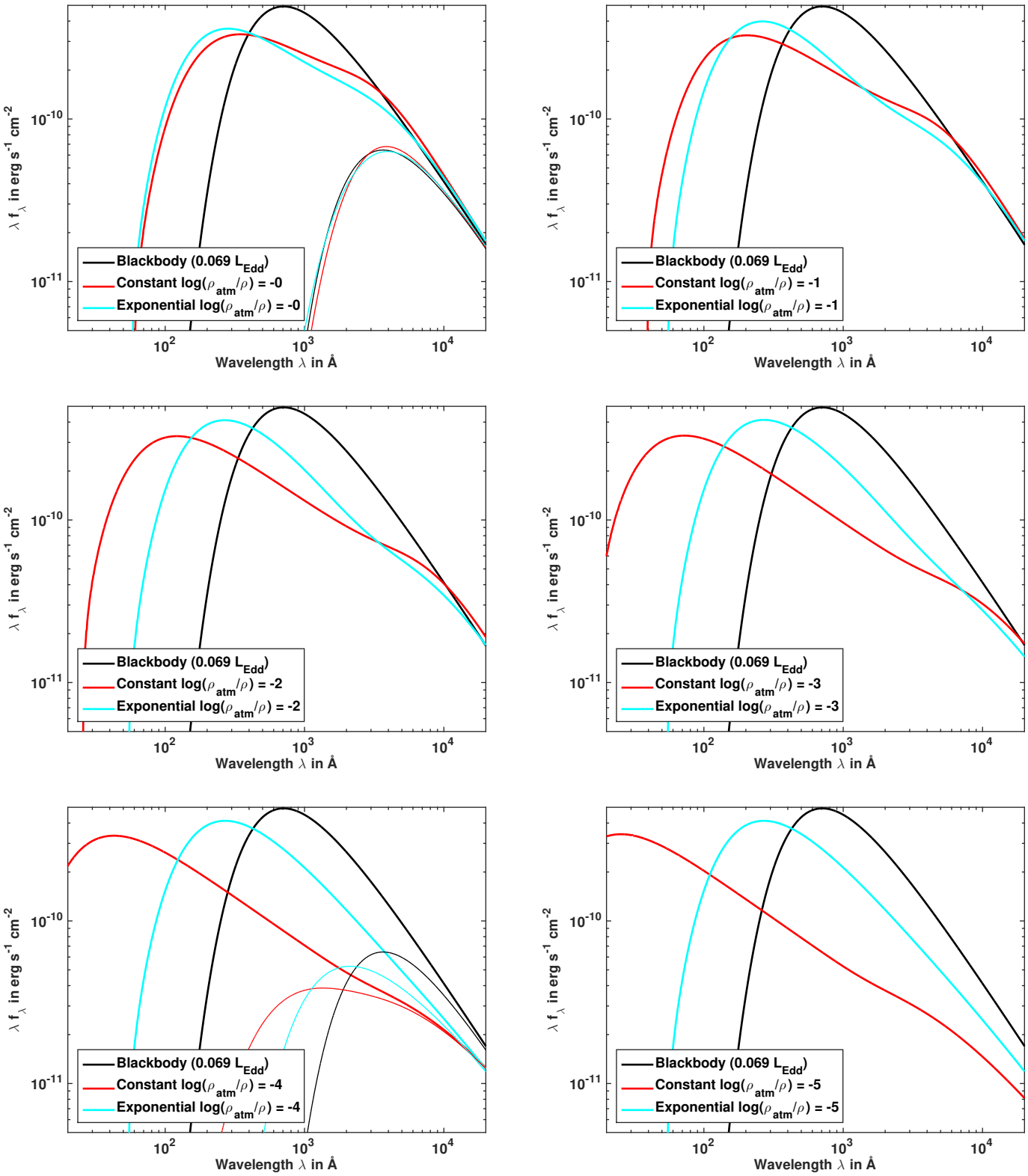

Figure 4. The predicted observed spectral energy distributions (SEDs) from face-on accretion disks with $L = 0.069 L_{\rm Edd}$ in NGC 5548. Panel layout and color key are as in Figure 1. The thin curves in the **upper left and lower left panels** show f_ν from $r > 60 R_{\rm Sch}$ only.

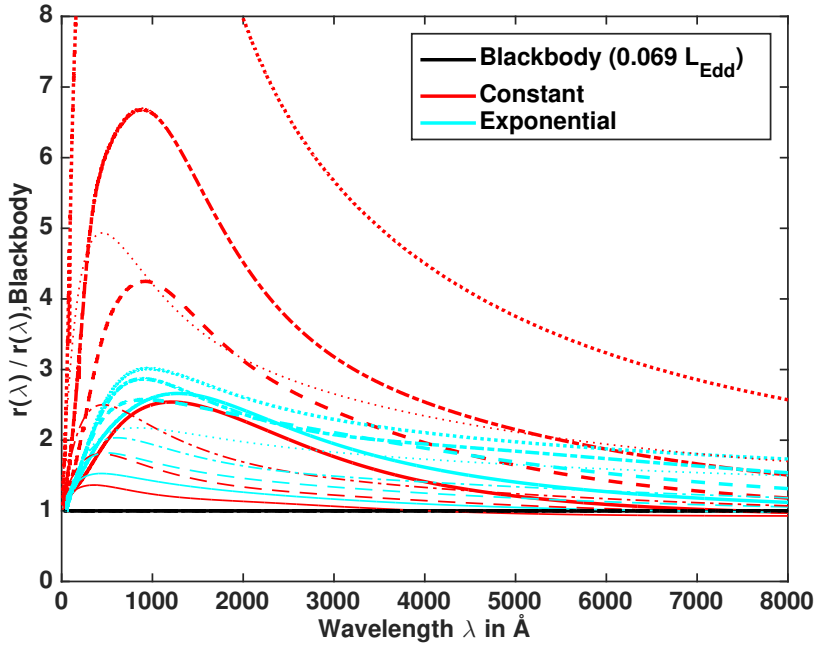

Figure 5. Mean radii $r(\lambda)$ divided by the corresponding $r(\lambda)$ for a blackbody disk, for scattering-atmosphere disks with constant density (red) and exponential density (cyan), all with $L = 0.069 L_{\rm Edd}$. **The curves shown are for** $\log(\rho_{atm}/\rho) = 0$ **(solid),** -1 **(dash-dotted),** -2 **(dashed), and** -4 **(dotted).** Heavy lines denote response-function-weighted radii and light lines denote flux-weighted radii.

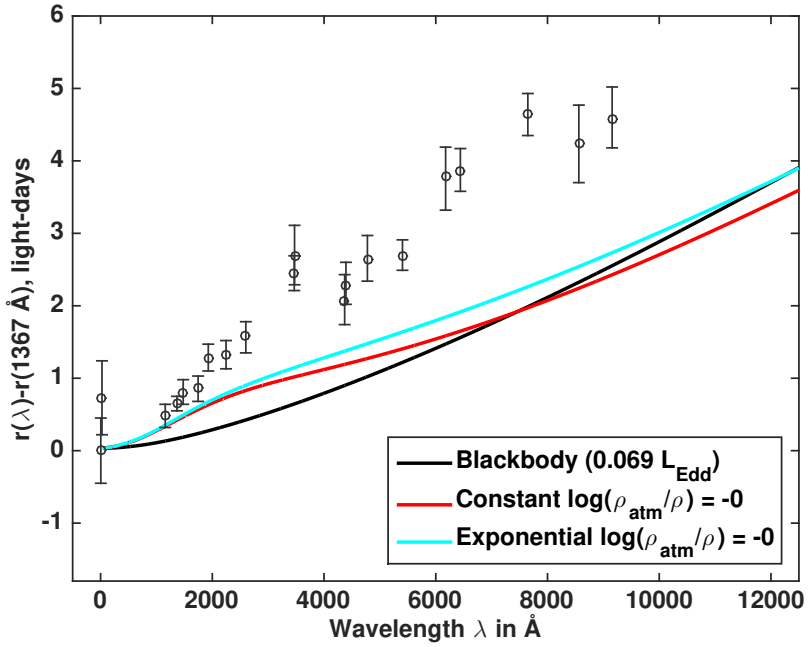

Figure 6. **In the same fashion as Figure 1 (see that caption for details), we plot the** *absolute* **wavelength-dependent relative disk reverberation time lag estimated from the response-function-weighted mean radius** $r(\lambda)$ **(solid lines) for blackbody disks (black) and scattering-atmosphere disks with constant density (red) and exponential density (cyan), all with** $\log(\rho_{atm}/\rho) = 0$**. Points from F16 are plotted assuming zero time delay for the Swift hard X-ray band. Even at the density of a standard thin disk, the deviation from blackbody emission due to electron scattering in the radiation-pressure-dominated region of the disk leads to reverberation lags which are up to two and a half times longer than predicted in the blackbody model (corresponding to the thick solid lines in Figure 5.)**

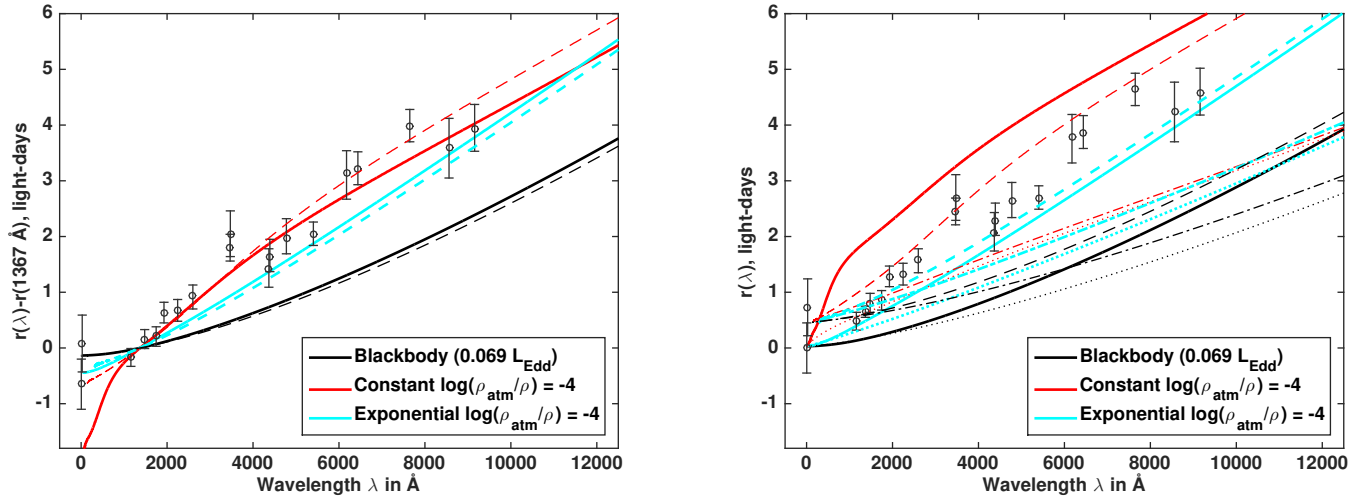

Figure 7. Left: in the same fashion as Figure 1 (see that caption for details), we plot the wavelength-dependent relative disk reverberation time lag estimated from the response-function-weighted mean radius $r(\lambda) - r$(1367 Å) (solid lines) for blackbody disks (black) and scattering-atmosphere disks with constant density (red) and exponential density (cyan), all with $\log(\rho_{atm}/\rho) = -4$. Dashed lines show the results considering disk radii $r > 60R_{\rm Sch}$ only. Right: response-function-weighted mean radii $r(\lambda)$ (absolute disk reverberation time lags) for blackbody disks (black) and scattering-atmosphere disks with constant density (red) and exponential density (cyan), all with $\log(\rho_{atm}/\rho) = -4$. Dashed lines show the results considering disk radii $r > 60R_{\rm Sch}$ only. Dotted and dot-dashed lines show flux-weighted radii for the full disk and for disk radii $r > 60R_{\rm Sch}$ only, respectively. Points from F16 are plotted assuming zero time delay for the Swift hard X-ray band.

Eigenbrod, A., Courbin, F., Meylan, G., et al. 2008, A&A, 490, 933

Fausnaugh, M. M., Denney, K. D., Barth, A. J., et al. 2016, ApJ, 821, 56

Frank, J., King, A., & Raine, D. J. 2002, Accretion Power in Astrophysics: Third Edition, 86

Gardner, E., & Done, C. 2017, MNRAS, 470, 3591

Hall, P. B., Noordeh, E. S., Chajet, L. S., Weiss, E., & Nixon, C. J. 2014, MNRAS, 442, 1090

Jiang, Y.-F., Davis, S. W., & Stone, J. M. 2016a, ApJ, 827, 10

Jiang, Y.-F., Green, P. J., Greene, J. E., et al. 2016b, ArXiv e-prints, arXiv:1612.08747

Kawaguchi, T., Pierens, A., & Huré, J.-M. 2004, A&A, 415, 47

Komatsu, E., Smith, K. M., Dunkley, J., et al. 2011, ApJS, 192, 18

Laor, A., & Davis, S. W. 2014, MNRAS, 438, 3024

Mehdipour, M., Kaastra, J. S., Kriss, G. A., Cappi, M. et al. 2015, A&A, 575, A22

Meier, D. L. 2012, Black Hole Astrophysics: The Engine Paradigm (Springer-Verlag)

Morgan, C. W., Kochanek, C. S., Morgan, N. D., & Falco, E. E. 2010, ApJ, 712, 1129

Mudd, D., Martini, P., Zu, Y., Kochanek, C., et al. 2017, ArXiv e-prints, arXiv:1711.11588

Novikov, I. D., & Thorne, K. S. 1973, in Black Holes (Les Astres Occlus), ed. C. Dewitt & B. S. Dewitt, 343–450

Pei, L., Fausnaugh, M. M., Barth, A. J., et al. 2017, ApJ, 837, 131

Proga, D. 2005, ApJL, 630, L9

Rauch, K. P., & Blandford, R. D. 1991, ApJL, 381, L39

Rybicki, G. B., & Lightman, A. P. 1986, Radiative Processes in Astrophysics (Wiley VCH), 320

Shakura, N. I., & Sunyaev, R. A. 1973, A&A, 24, 337

Shappee, B. J., Prieto, J. L., Grupe, D., et al. 2014, ApJ, 788, 48

Slone, O., & Netzer, H. 2012, MNRAS, 426, 656

Starkey, D., Horne, K., Fausnaugh, M., et al. 2017, ApJ, 835, 65

Tao, T., & Blaes, O. 2013, ApJ, 770, 55

Woo, J.-H., & Urry, C. M. 2002, ApJ, 579, 530

Zel'dovich, Y. B., & Shakura, N. I. 1969, Soviet Ast., 13, 175